Supporting Information

Synergy of W doping and oxygen vacancies engineering on d-band centers modulation for enhanced gas sensing performance

Yushu Shi [a, b, c], Tongyao Liu [a*], Riming Hu [a], Huiyan Xu [a], Chengxiang Yang [a], Likai Yang [a], Liang Feng [b, c*], Xuchuan Jiang [a*]

[a]Institute for Smart Materials & Engineering, University of Jinan, 250022, Jinan, PR China

[b] Department of Instrumentation and Analytical Chemistry, CAS Key Laboratory of Separation Science for Analytical Chemistry, Dalian Institute of Chemical Physics, Chinese Academy of Sciences, Dalian 116023, PR China

[c] University of Chinese Academy of Sciences, Beijing 100049, PR China

[*]Corresponding author

E-mail address: ism_liuty@ujn.edu.cn (T.Y. Liu), fengl@dicp.ac.cn (L. Feng), sm_jiangxc@ujn.edu.cn (X.C. Jiang).

Theoretical calculation section

All the density functional theory calculations were performed by using the Vienna ab initio Simulation Program (VASP) [1, 2]. The generalized gradient approximation (GGA) in the Perdew-Burke-Ernzerhof (PBE) form and a cutoff energy of 500 eV for planewave basis set were adopted [3]. A $3 \times 3 \times 1$ Monkhorst-Pack [4] grid was used for sampling the Brillouin zones at structure optimization. The ion-electron interactions were described by the projector augmented wave (PAW) method [5]. To assess the adsorption properties of triethylamine on W-doped $NiCo_2O_4$, the surface model of $\sqrt{2} \times \sqrt{2}$ $NiCo_2O_4(111)$ supercell with 112 atoms is employed. The convergence criteria of structure optimization were chosen as the maximum force on each atom less than 0.01 eV/Å with an energy change less than 1×10^{-5} eV.

The oxygen vacancy formation energy (E_v) was calculated as follows:

$E_v = E_O + \mu_O - E_p$

where E_O is the energies for $NiCo_2O_4$ with oxygen defect, the chemical potentials (μ) of oxygen atom are derived from the oxygen molecule.

Furthermore, the adsorption energy of TEA on the surface is defined as follow:

$E_{ad} = E_T - E_s - E_m$

where E_T, E_s, and E_m are the energies of whole adsorption system, adsorption substrates, and TEA molecules, respectively.
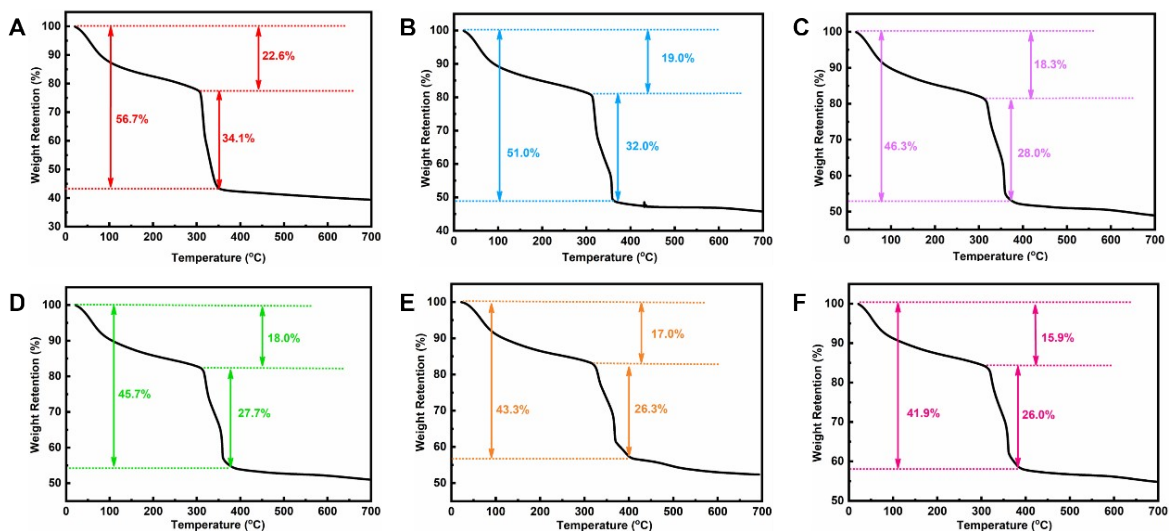
Figure S1. The TGA curves of different amount W doping (A) NiCoW-0, (B) NiCoW-5, (C) NiCoW-10, (D) NiCoW-15, (E) NiCoW-20, (F) NiCoW-25.

All the samples display two distinct stages related to weight loss during annealing. The former that occurs at the beginning of heating was ascribed to the removal of water molecules physically adsorbed on the particle surface, whereas the latter occurs at approximately 350 °C, which could be attributed to the elimination or decomposition of organic component(s) in the precursor. However, with an increase in the dopant amount, the weight loss gradually decreases, further confirming the successful doping of W into $NiCo_2O_4$.
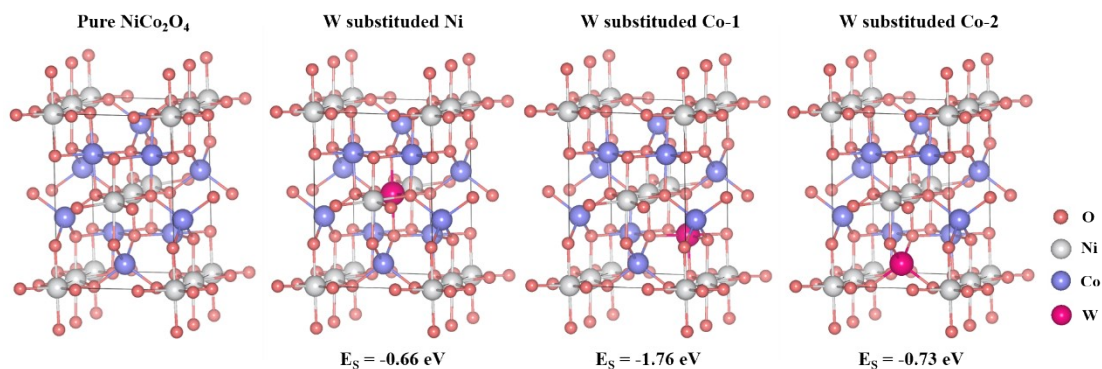
Figure S2. DFT calculation models regarding the different doping positions of W.
Note: Ni substituted Co-1：W atoms replace the Co atoms in CoO_6 polyhedron,
Ni substituted Co-2：W atoms replace the Co atoms in CoO_4 polyhedron.

The substitution energy (E_s) was calculated by varying the W-doping position. As illustrated in **Figure S2**, the "Ni substituted Co-1" model (W atoms replace Co atoms in the CoO_6 polyhedron) exhibited the lowest E_s among several different NiCoW models. This indicated that the doped W atoms preferred to replace Co atoms coordinated with six O atoms, consistent with the direction of peak shift in XRD pattern.
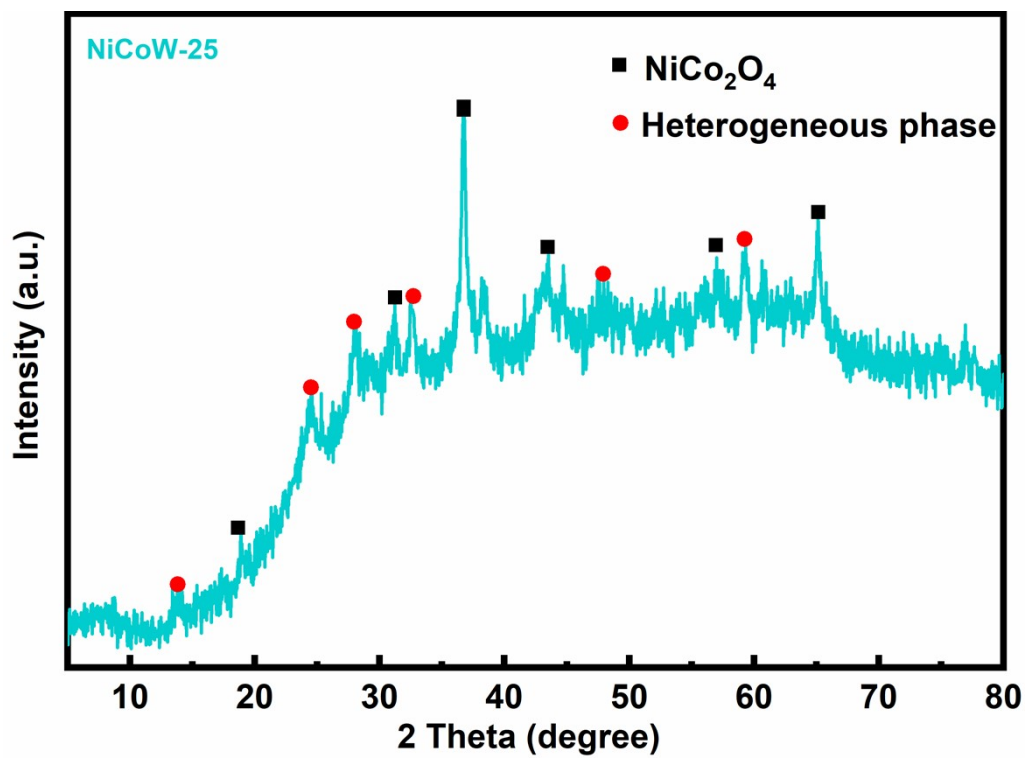
Figure S3. The XRD pattern of NiCoW-25

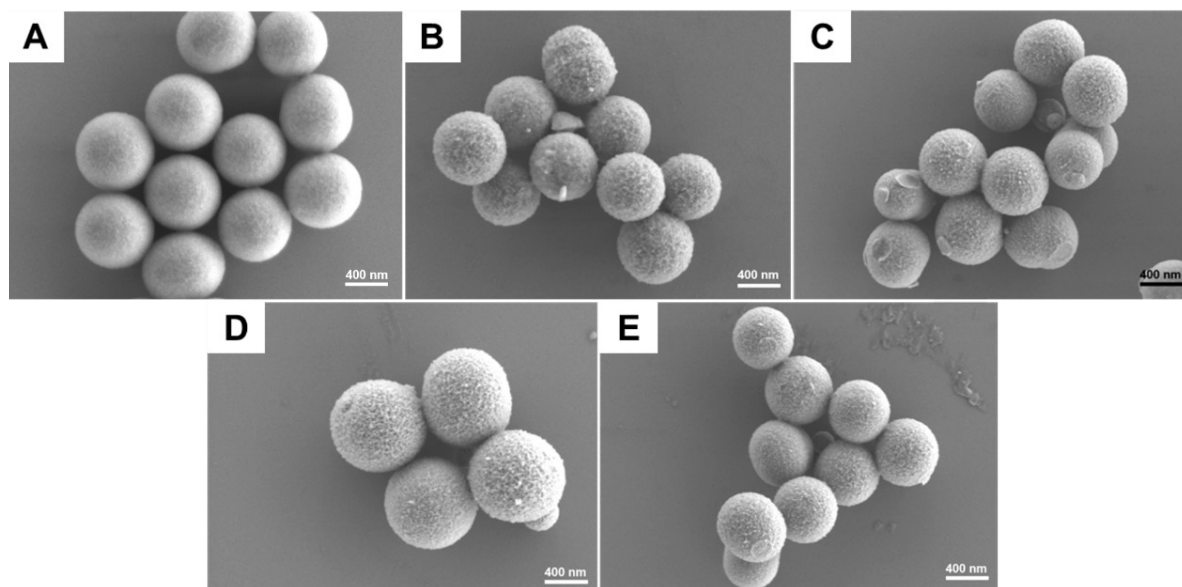The heterogeneous phases are marked by red dots.

Figure S4. The glycerate precursor FE-SEM of (A) NiCoW-0, (B) NiCoW-5, (C) NiCoW-10, (D) NiCoW-15, (E) NiCoW-25.
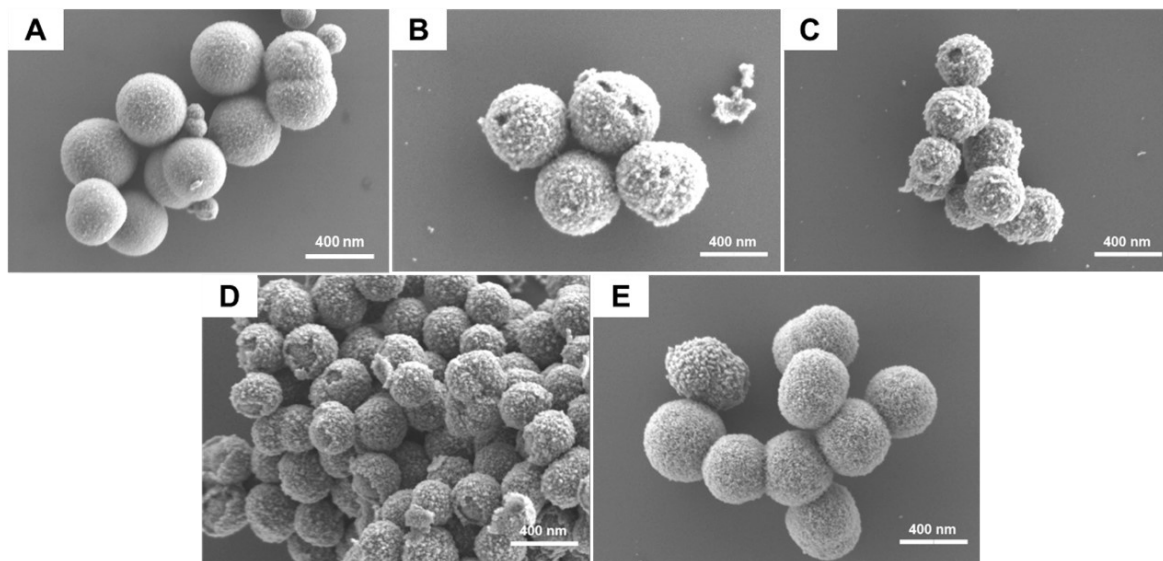
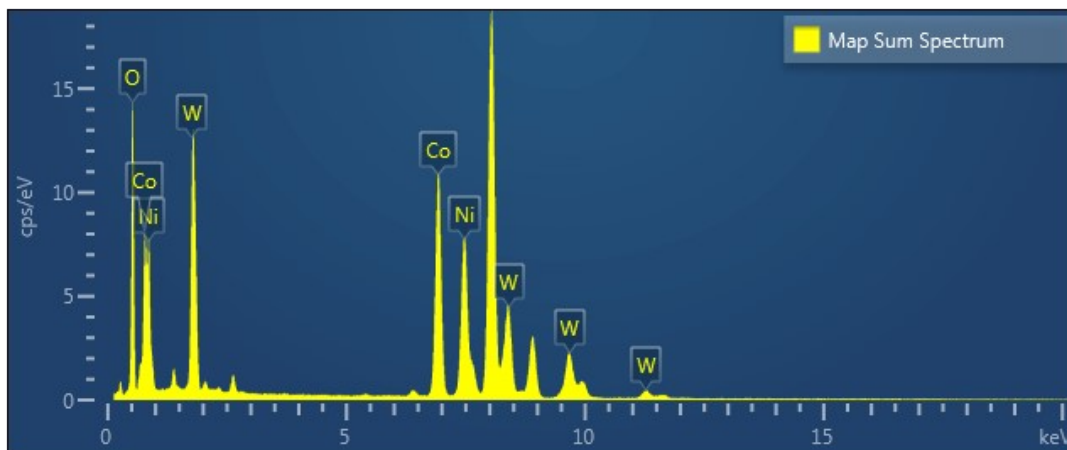**Figure S5.** The FE-SEM images of (A) NiCoW-0, (B) NiCoW-5, (C) NiCoW-10, (D) NiCoW-15, (E) NiCoW-25.
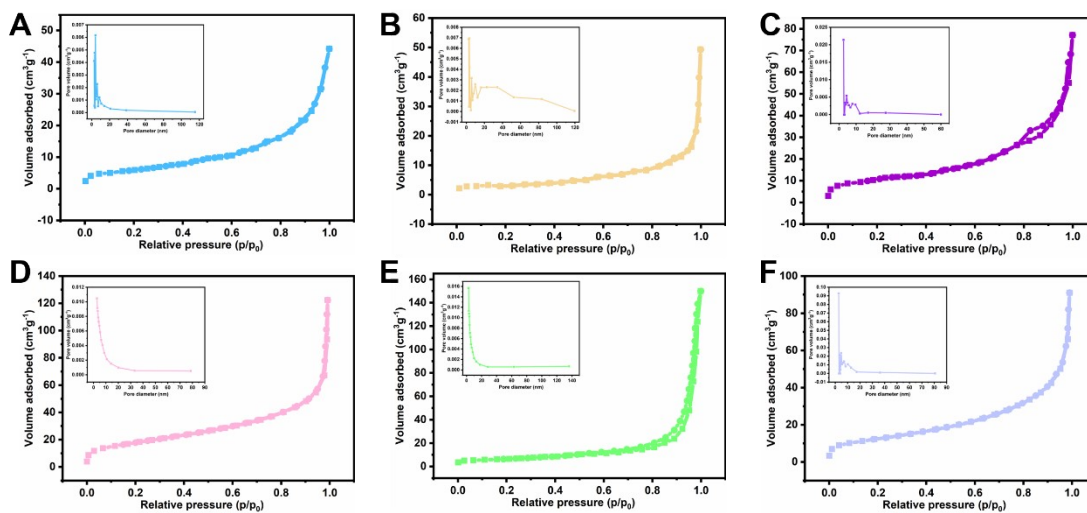
Figure S6. EDS image of NiCoW-20.

Figure S7. The nitrogen adsorption-desorption isotherms and pore sizes distribution curves of glycerate precursor (A) NiCoW-0, (B) NiCoW-5, (C) NiCoW-10, (D) NiCoW-15, (E) NiCoW-20, (F) NiCoW-25.
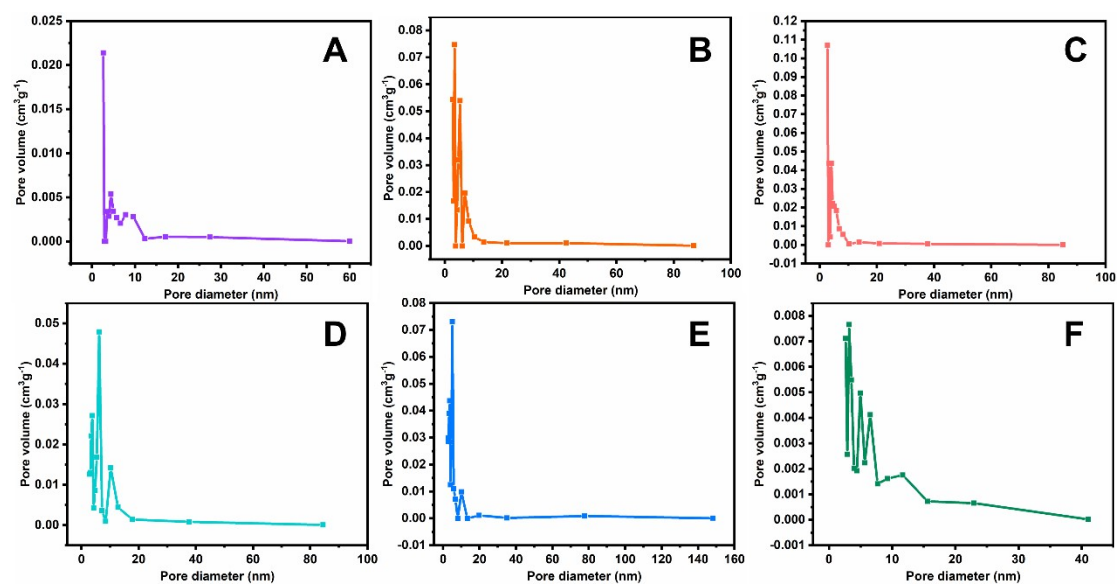
Figure S8. Pore size distribution of (A) NiCoW-0, (B) NiCoW-5, (C) NiCoW-10, (D) NiCoW-15, (E) NiCoW-20, (F) NiCoW-25.
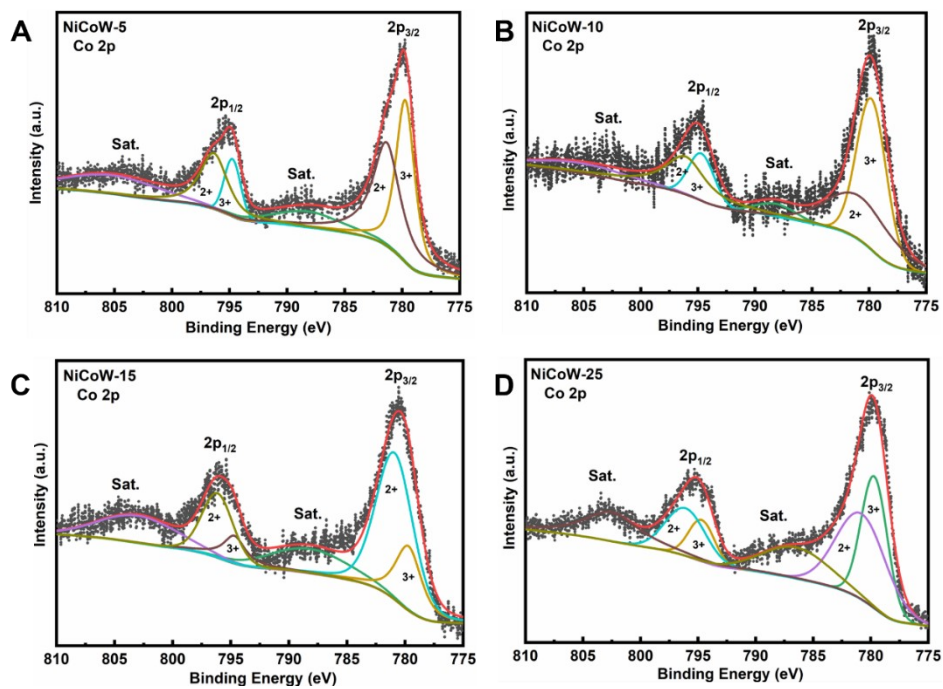
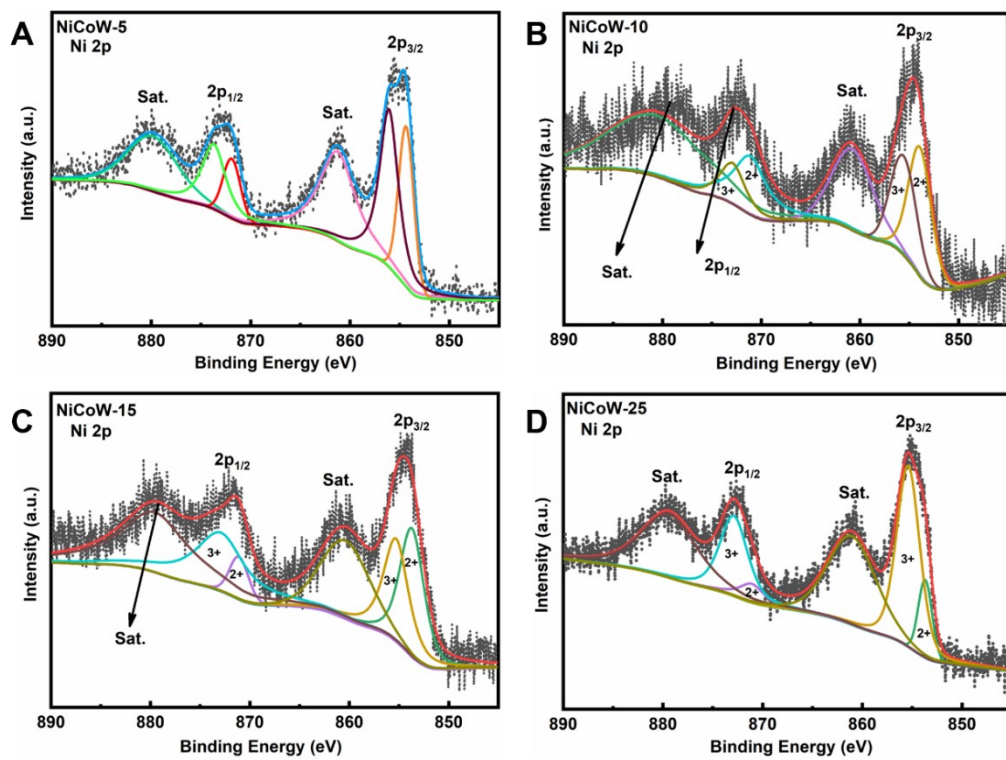**Figure S9.** The Co XPS fine spectra (A) NiCoW-5, (B) NiCoW-10, (C) NiCoW-15, (D) NiCoW-25.

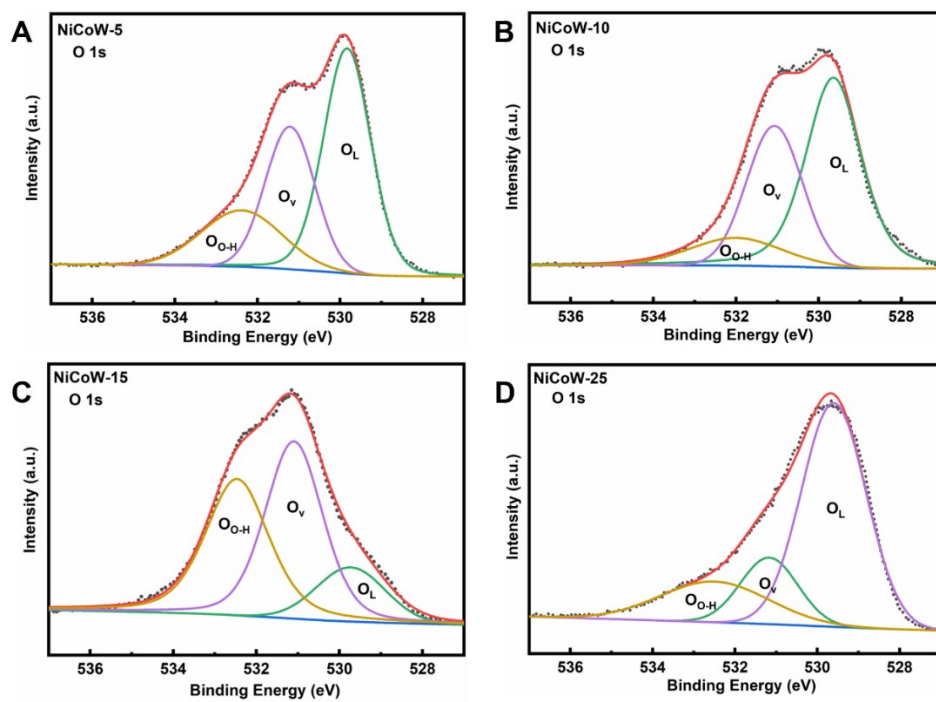**Figure S10.** The Ni XPS fine spectra (A) NiCoW-5, (B) NiCoW-10, (C) NiCoW-15, (D) NiCoW-25.

Figure S11. The O XPS fine spectra (A) NiCoW-5, (B) NiCoW-10, (C) NiCoW-15, (D) NiCoW-25.
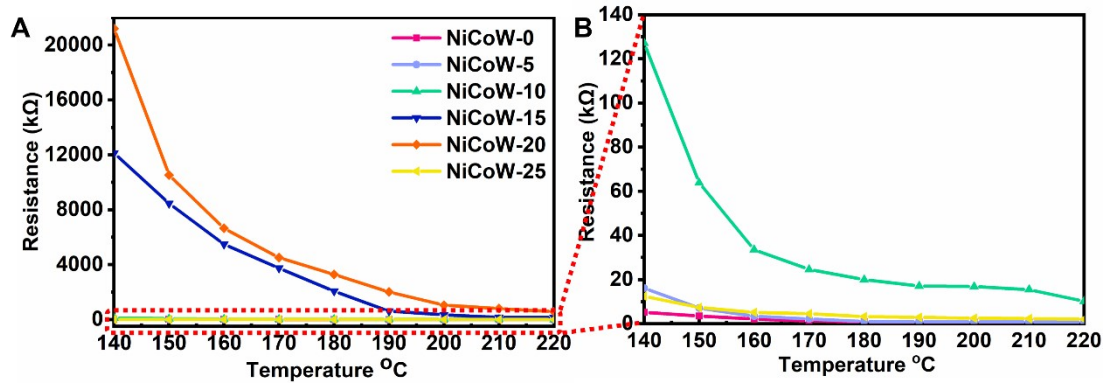
Figure S12. Variation curves of different samples with temperature.

The curve of the baseline resistance at different temperatures is shown in **Figure S12**. Evidently, the baseline resistance of the sensor decreases with increasing temperature, which is characteristic of a p-type semiconductor. At the same operating temperature, the baseline resistance Ra gradually increases with W-doping content (**Figure S12**), which was attributed to the increased oxygen vacancies and carrier concentration due to the W doping. Therefore, the NiCoW-20 can capture more carriers from its conduction band, resulting in the highest resistance of the whole samples. In contrast, owing to the formation of a heterogeneous structure, NiCoW-25 exhibits an extremely low resistance compared to the other NiCoW samples, which is consistent with previous characterization results.
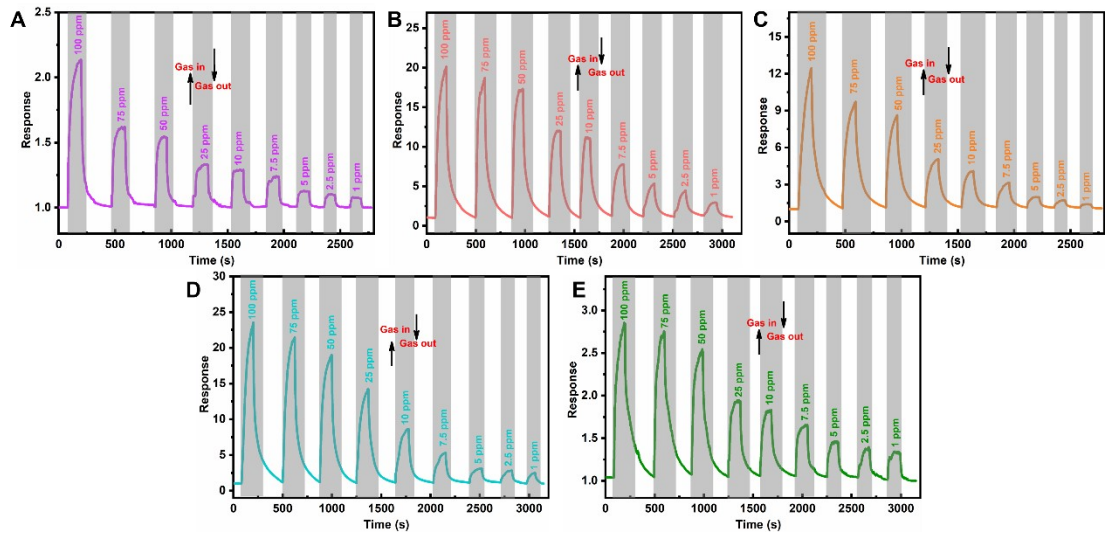
Figure S13. The dynamic response curve showing sensors performance (A) NiCoW-0, (B) NiCoW-5, (C) NiCoW-10, (D) NiCoW-15, (E) NiCoW-25.
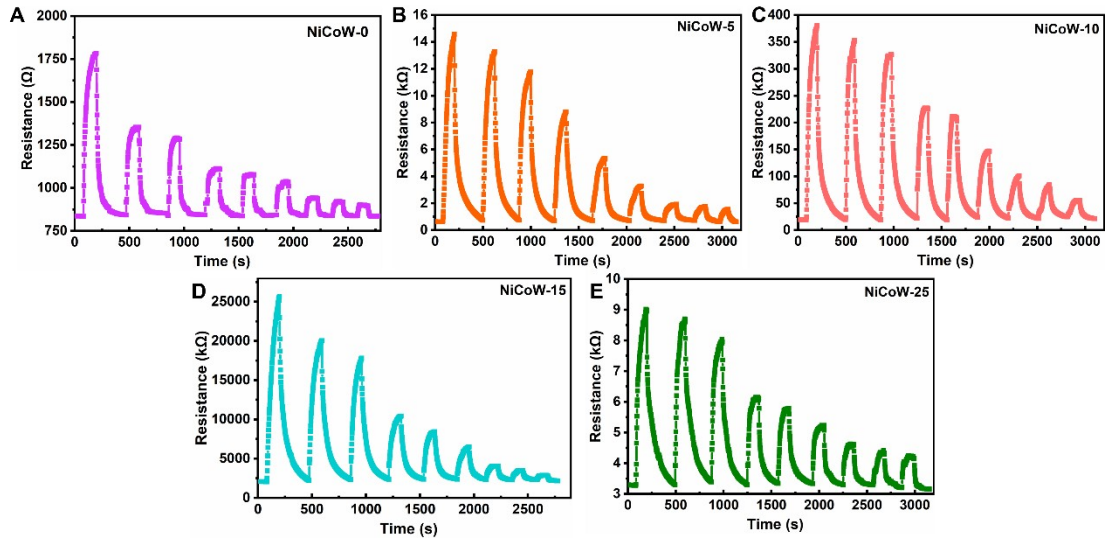
Figure S14. The dynamic resistance curves of (A) NiCoW-0, (B) NiCoW-5, (C) NiCoW-10, (D) NiCoW-15, (E) NiCoW-25.

This indicates that the baseline resistance of the sensor remains stable during long-term testing.
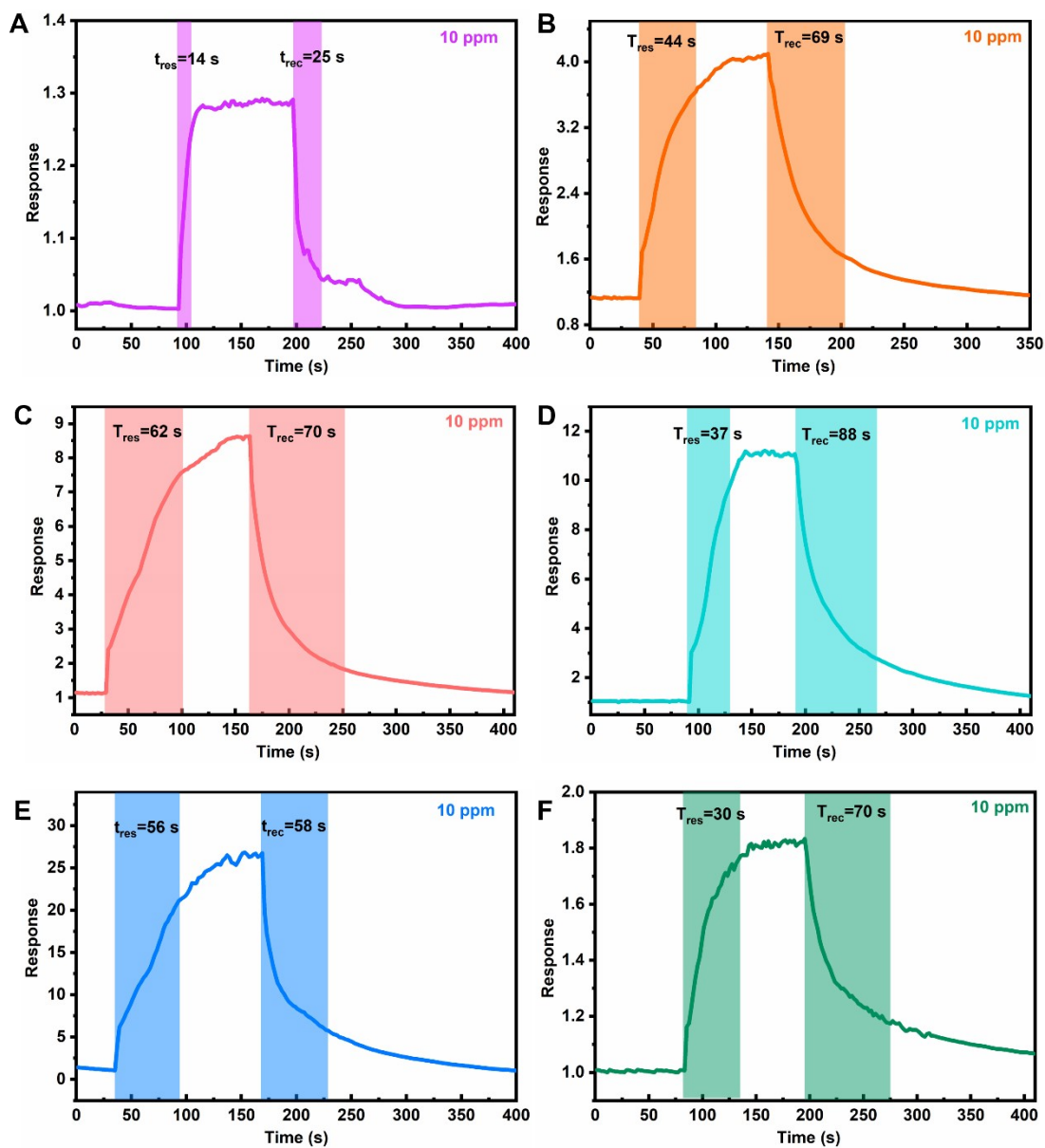
Figure S15. Response and recovery time of (A) NiCoW-0, (B) NiCoW-5, (C) NiCoW-10, (D) NiCoW-15, (E) NiCoW-20, (F) NiCoW-25.
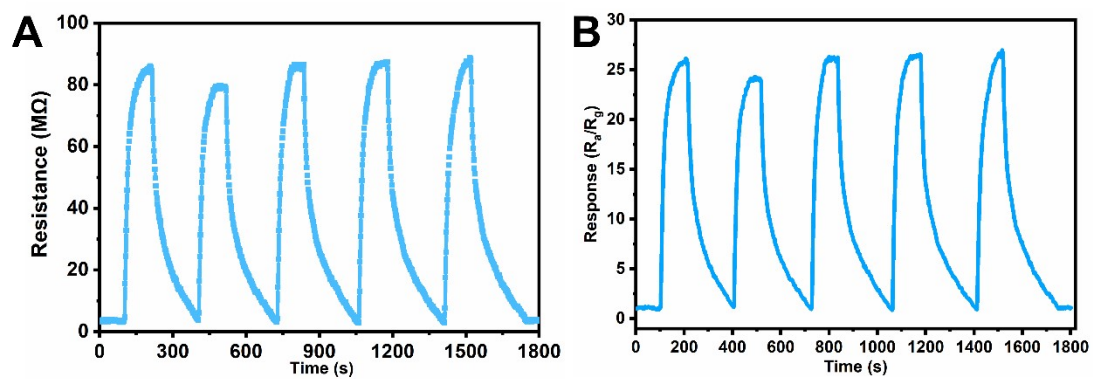
Figure S16. Cycle stability curve (5 cycles) of NiCoW-20 to 10 ppm TEA at 180 °C. The dynamic resistance curves (A) and the dynamic response curve (B).

Over the course of 5 cycles, the sensor exhibits good cycling stability while the baseline resistance also remains relatively stable.
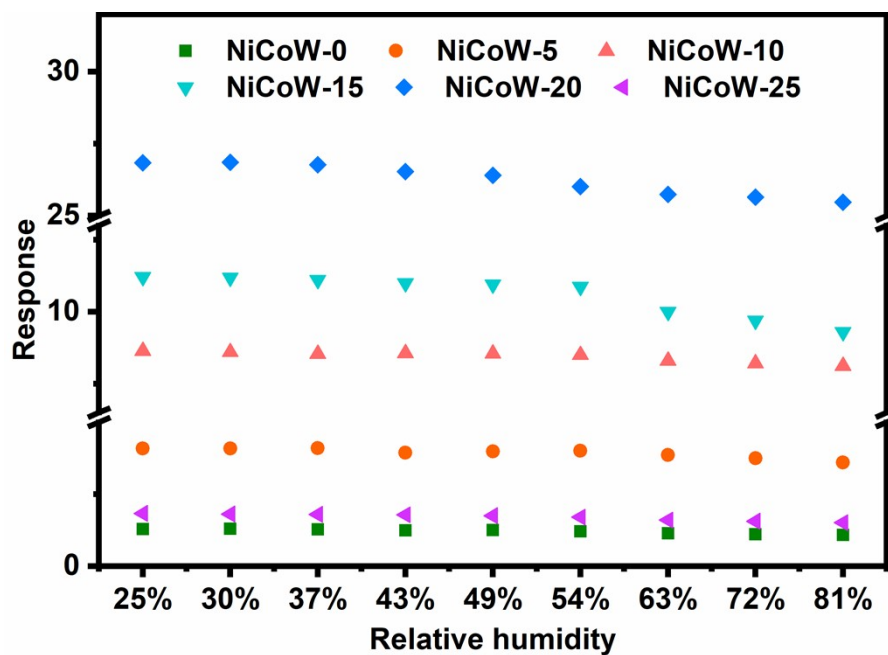
Figure S17. Responses of the sensors to 10 ppm TEA as a function of the relative humidity at 180 °C.

As can be seen from the **Figure S17**, the performance of the sensors decreases with the increase of humidity, but remains stable in general. It indicates that the sensors could be applied in the real environment.

Table S1. Preparation and detection of W element by XPS and ICP analysis

Sample name	Designed (Ni+Co)/W (at. %)	XPS analysed (Ni+Co)/W (at. %)	ICP analysed (Ni+Co)/W (at. %)
NiCoW-5	3.6	10.62	4.05
NiCoW-10	7.2	11.89	6.94
NiCoW-15	10.8	12.70	10.73
NiCoW-20	14.4	14.45	13.98

Table S2. The calculated BET specific-surface areas of the samples

Sample name	BET specific-surface areas ($m^2 \ g^{-1}$)
NiCoW-0	57.36
NiCoW-5	65.75
NiCoW-10	74.49
NiCoW-15	89.48
NiCoW-20	98.45
NiCoW-25	51.15

Table S3. The content of O_V for all samples

Sample name	The content of O_V (%)
NiCoW-0	27.6
NiCoW-5	31.9
NiCoW-10	37.8
NiCoW-15	41.8
NiCoW-20	49.3
NiCoW-25	16.8

XPS is a materials surface analysis method, so such a high concentration of oxygen defects refers to the superficial oxygen vacancies on the surface of the material. Based on this, the whole crystal structure of the materials can be still maintained.

And this widespread presence of oxygen vacancies on the surface of the material facilitates the adsorption of gases on the surface of the sensing material thus enhancing the performance of the sensor.

Table S4. The substitution energy (E_s) of the W-doping position in $NiCo_2O_4$.

W-doping position	The substitution energy (eV)
W substituted Ni	-0.66
W substituted Co-1	-1.76
W substituted Co-2	-0.73

DFT calculations indicate that the doped W atoms preferred to replace Co atoms coordinated with six O atoms whose valence state is +3. Meanwhile, the results are consistent with the direction of XRD shift.

Table S5. Oxygen vacancy formation energy of pristine $NiCo_2O_4$ and W doped $NiCo_2O_4$.

Sample	Vacancy formation energy (eV)	
pristine $NiCo_2O_4$	-1.86	-2.04
W doped $NiCo_2O_4$	-1.83	-1.85

DFT calculations indicate that the introduction of W into $NiCo_2O_4$ can reduce the formation energy for oxygen vacancy (1.86 eV and 2.04 eV for pristine $NiCo_2O_4$ vs. 1.83 eV and 1.85 eV for W doped $NiCo_2O_4$), which confirms the role of W dopants in promoting the formation of oxygen vacancies. Moreover, the DFT calculations are consistent with XPS and EPR characterization.

Table S6. Comparison of the gas-sensing properties of various metal oxide-based sensors to TEA.

Materials	T (°C)	c (ppm)	$S_{g/a}$ (R_g/R_a)	t_{res}/t_{rec}(s)	Ref.
In$_2$O$_3$-NiO hollow sphere	200	100	33.9	140/68	[6]
Tortoise shell-like porous NiCo$_2$O$_4$ nanoplate	220	100	~2.6	33/42	[7]
Hierarchical kiwifruit-like ZnO/ZnFe$_2$O$_4$	200	100	40.15	32/41	[8]
V$_2$O$_5$ hollow spheres	370	100	7.3	40/125	[9]
MoS$_2$/ZnO	200	100	23.57	103/134	[10]
NC-ZnSnO$_3$	350	100	57.5	4/1040	[11]
Co$_3$O$_4$@MnO$_2$	250	100	9.13	—	[12]
BiVO$_4$/rGO hybrids	180	10	5.9	—	[13]
CuO	200	100	~9	21/19	[14]
Al$_2$O$_3$/α-Fe$_2$O$_3$ composite	250	100	15.19	1/17	[15]
rGO/Fe$_2$O$_3$ nanocomposites	280	50	24	2/7	[16]
ZnO/ZnCo$_2$O$_4$	220	100	5.12	8/65	[17]
W-NiCo$_2$O$_4$ Nanospheres	180	10	26.83	56/58	This work

References

[1] G.Kresse, J. Furthmüller, Efficiency of Ab initio total energy calculations for metals and semiconductors using a plane-wave basis set, Comput. Mater. Sci. 1 (1996) 15-50.

[2] G.Kresse, J. Furthmüller, Efficiency iterative schemes for Ab initio total-energy calculations using a plane-wave basis set, Phys. Rev. B. 16 (1996) 11169-11186.

[3] J.P. Perdew, K. Burke, M. Ernzerhof, Generalized gradient approximation made simple, Phys. Rev. Lett. 18 (1996) 3865-3868.

[4] H.J. Monkhorst, J.D. Pack, Special point for Brillouin-zone integrations, Phys. Rev. B. 13 (12) (1976) 5188-5192.

[5] P.E. Blöchl, Projector augmented-wave method, Phys. Rev. B. 50 (24) (1994) 17953-17979.

[6] Q. Yu, R. Jin, L. Zhao, T. Wang, F. Liu, X. Yan, et al., MOF-Derived Mesoporous and Hierarchical Hollow-Structured In_2O_3-NiO Composites for Enhanced Triethylamine Sensing, ACS Sens, 6(2021), 3451-3461.

[7] Y. Zhao, X. Yuan, Y. Sun, Q. Wang, X.-Y. Xia, B. Tang, Facile synthesis of tortoise shell-like porous $NiCo_2O_4$ nanoplate with promising triethylamine gas sensing properties, Sens Actuators, B, 323(2020) 128663.

[8] S. Li, Y. Zhang, L. Han, X. Li, Y. Xu, Hierarchical kiwifruit-like $ZnO/ZnFe_2O_4$ heterostructure for high-sensitive triethylamine gaseous sensor, Sens Actuators, B, 344(2021) 130251.

[9] M. Wu, X. Zhang, S. Gao, X. Cheng, Z. Rong, Y. Xu, et al., Construction of monodisperse vanadium pentoxide hollow spheres via a facile route and triethylamine sensing property, CrystEngComm, 15(2013) 10123-31.

[10] X. Xu, S. Wang, W. Liu, Y. Chen, S. Ma, P. Yun, An excellent triethylamine (TEA) sensor based on unique hierarchical MoS_2/ZnO composites composed of porous microspheres and nanosheets, Sens Actuators, B, 333(2021) 129616.

[11] B.S. Sá, C.A. Zito, T.M. Perfecto, D.P. Volanti, Porous $ZnSnO_3$ nanocubes as a triethylamine sensor, Sens Actuators, B, 338(2021) 129869.

[12] Y. Liang, Y. Yang, K. Xu, T. Yu, Q. Peng, S. Yao, et al., Controllable preparation

of faceted Co_3O_4 nanocrystals@MnO_2 nanowires shish-kebab structures with enhanced triethylamine sensing performance, Sens Actuators, B, 304(2020) 127358.

[13] S. Bai, L. Sun, J. Sun, J. Han, K. Zhang, Q. Li, et al., Pine dendritic bismuth vanadate loaded on reduced graphene oxide for detection of low concentration triethylamine, J Colloid Interface Sci, 587(2021) 183-91.

[14] W. Geng, Z. Ma, Y. Zhao, J. Yang, X. He, L. Duan, et al., Morphology-Dependent Gas Sensing Properties of CuO Microstructures Self-Assembled from Nanorods, Sens Actuators, B, 325(2020) 128775.

[15] L. Guo, C. Wang, X. Kou, N. Xie, F. Liu, H. Zhang, et al., Detection of triethylamine with fast response by Al_2O_3/α-Fe_2O_3 composite nanofibers, Sens Actuators, B, 266(2018) 139-48.

[16] Q. Wei, J. Sun, P. Song, J. Li, Z. Yang, Q. Wang, MOF-derived α-Fe_2O_3 porous spindle combined with reduced graphene oxide for improvement of TEA sensing performance, Sens Actuators, B, 304(2020) 127306.

[17] Y. Li, N. Luo, G. Sun, B. Zhang, H. Jin, L. Lin, et al., Synthesis of porous nanosheets-assembled ZnO/$ZnCo_2O_4$ hierarchical structure for TEA detection, Sens Actuators, B, 287(2019) 199-208.